

Robust Lithium–Sulfur Batteries Enabled by Highly Conductive WSe₂-Based Superlattices with Tunable Interlayer Space

Chaoqi Zhang, Ban Fei, Dawei Yang, Hongbing Zhan,* Jiaao Wang,* Jiefeng Diao, Junshan Li, Graeme Henkelman, Daoping Cai, Jordi Jacas Biendicho, Joan Ramon Morante, and Andreu Cabot*

Superlattices are rising stars on the horizon of energy storage and conversion, bringing new functionalities; however, their complex synthesis limits their large-scale production and application. Herein, a simple solution-based method is reported to produce organic–inorganic superlattices and demonstrate that the pyrolysis of the organic compound enables tuning their interlayer space. This strategy is exemplified here by combining polyvinyl pyrrolidone (PVP) with WSe₂ within PVP/WSe₂ superlattices. The annealing of such heterostructures results in N-doped graphene/WSe₂ (NG/WSe₂) superlattices with a continuously adjustable interlayer space in the range from 10.4 to 21 Å. Such NG/WSe₂ superlattices show a metallic electronic character with outstanding electrical conductivities. Both experimental results and theoretical calculations further demonstrate that these superlattices are excellent sulfur hosts at the cathode of lithium–sulfur batteries (LSB), being able to effectively reduce the lithium polysulfide shuttle effect by dual-adsorption sites and accelerating the sluggish Li–S reaction kinetics. Consequently, S@NG/WSe₂ electrodes enable LSBs characterized by high sulfur usages, superior rate performance, and outstanding cycling stability, even at high sulfur loadings, lean electrolyte conditions, and at the pouch cell level. Overall, this work not only establishes a cost-effective strategy to produce artificial superlattice materials but also pioneers their application in the field of LSBs.

1. Introduction

Since the discovery of graphene in 2004, the 2D material family has grown rapidly.^[1,2] A plethora of monolayered 2D materials produced by exfoliating bulk layered materials have demonstrated fascinating physical and chemical properties.^[3] Besides, these monolayer nanosheets have been combined and stacked together with extraordinary control to form new 2D heterostructures and superlattice materials.^[4–6] These artificial structures further enrich the family of 2D materials with new functionalities, providing unprecedented performances when applied to the fields of light-emitting diodes, field-effect transistors, quantum devices, as well as energy storage and conversion, among others.^[7] Since the possible combinations are virtually unlimited, numerous new 2D superlattices with unique properties and functionalities are yet to be designed, engineered, and tested in different application fields.

C. Q. Zhang, B. Fei, H. B. Zhan, D. P. Cai
College of Materials Science and Engineering
Fuzhou University
No.2, Xueyuan Road, Minhou County, Fuzhou City, Fujian Province
350108, China
E-mail: hbzhan@fzu.edu.cn

C. Q. Zhang, D. W. Yang, J. J. Biendicho, J. R. Morante, A. Cabot
Catalonia Institute for Energy Research – IREC
Sant Adrià de Besòs, Barcelona 08930, Spain
E-mail: acabot@irec.cat

C. Q. Zhang, D. W. Yang, J. R. Morante
Department of Electronic and Biomedical Engineering
Universitat de Barcelona
Barcelona 08028, Spain

 The ORCID identification number(s) for the author(s) of this article can be found under <https://doi.org/10.1002/adfm.202201322>.

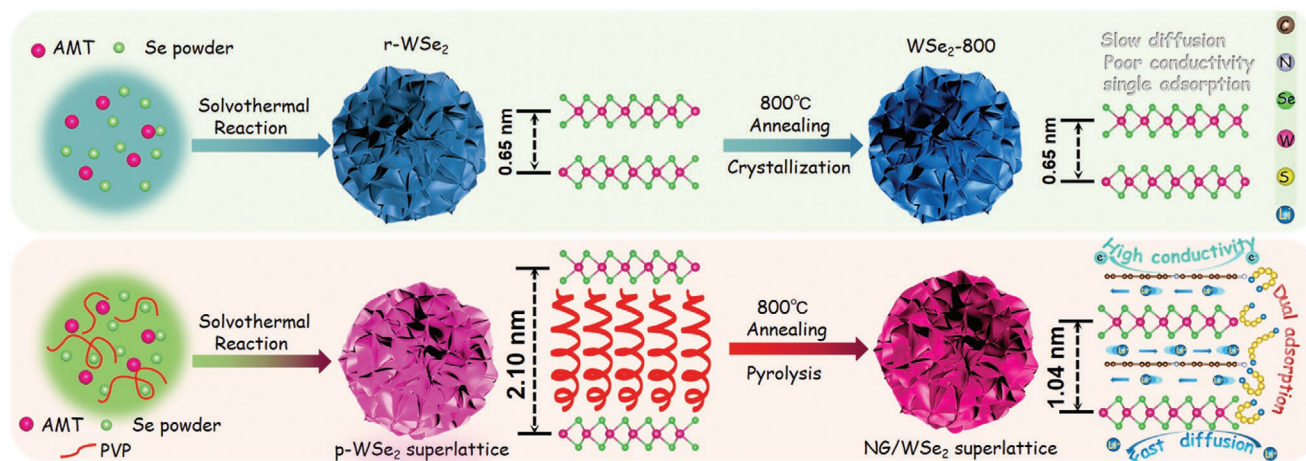
B. Fei
School of Chemistry
Trinity College Dublin
Dublin 2, Ireland

J. A. Wang, J. F. Diao, G. Henkelman
Department of Chemistry and the Oden Institute for Computational Engineering and Sciences
The University of Texas at Austin
Austin, TX 78712-0165, USA
E-mail: wangjiaao0720@utexas.edu

J. S. Li
Institute of Advanced Study
Chengdu University
Chengdu 610106, China

A. Cabot
Catalan Institution for Research and Advanced Studies – ICREA
Pg. Lluís Companys 23, Barcelona 08010, Spain

DOI: 10.1002/adfm.202201322



Scheme 1. Schematic illustration of the synthetic procedure used to produce NG/WSe₂ superlattice.

Despite the advantages of 2D superlattice materials, their large-scale synthesis is still challenging, which limits their commercial application. Superlattice structures are generally produced by low throughput methodologies, such as layer-by-layer mechanical assembly or epitaxial growth by chemical vapor deposition, which makes them incompatible with material-intensive applications such as energy storage.^[8,9] Other proposed methodologies, such as the flocculating self-assembly of solution-dispersed nanosheets, still rely on the laborious precursor exfoliation step that limits the process scale-up.^[5,10] Thus the development of alternative cost-effective methods for the mass production of functional 2D superlattice materials is essential for their commercial implementation.

In the electrochemistry field, superlattice materials offer the unique advantages of tuneable interlayer spacing and improved conductivity on the base of an adjustable electronic band structure.^[11,12] The former can provide fast 2D diffusion channels for the transport of reactants,^[13] and the latter allows optimizing charge transport/injection and electrocatalytic activity.^[10,14] In the field of energy storage, proper tailoring of the interlayer spacing has great potential for the engineering of the next generation of hybrid ion supercapacitors and secondary batteries based on Mg/K/Zn for instance.^[7] However, effective optimization of the material's functional properties requires a precise tuning of its structural and chemical properties that has remained elusive. While superlattice materials with enlarged interlayer spacing have been reported,^[5] a continuous and precise adjustment of the interlayer spacing to provide ion-selective 2D channels is yet to be accomplished.

Among other exciting applications, the unique characteristics of superlattice materials have the potential to solve the current limitations of lithium–sulfur batteries (LSBs). Recently, the Sasaki group reported Nb₃O₈/graphene superlattice as a three-in-one cathode host to prevent the lithium polysulfide (LiPS) shuttle effect, accelerate LiPS conversion, and promote Li₂S nucleation, delivering superior electrochemical performance.^[15] In terms of host material design, carbon materials and transitional metal dichalcogenides have been extensively investigated as cathode sulfur hosts to boost the performance of LSBs, but a single component host cannot meet the strict requirements

of LSBs.^[16–19] While graphene and other carbon supports can provide high specific surface area and electrical conductivity, their nonpolar surfaces are unable to anchor the soluble LiPS and catalyze their reaction.^[20,21] On the other hand, dichalcogenides provide polar surfaces to effectively anchor LiPS and catalyze LiPS conversion,^[22–25] but are characterized by moderate electrical conductivities, especially those characterized by layered structures with weak van der Waals interlayer bonding that shields electron transport between layers.^[26] Because graphene and metal dichalcogenides show highly complementary properties and limitations as sulfur hosts in LSB cathodes, the development of graphene-transition metal dichalcogenide superlattices that combine the complementary advantages of the two materials would have great potential to improve LSB performance. Nevertheless, surprisingly, such superlattice materials have never been designed, engineered, optimized, or tested within an LSB.

Herein, we report a simple two-step method for the cost-effective production of highly conductive N-doped graphene/WSe₂ (NG/WSe₂) superlattices. First, a scalable solvothermal method is employed to produce hybrid organic-inorganic polymer-WSe₂ superlattices with intercalated polyvinyl pyrrolidone (PVP). After a subsequent calcination step, NG/WSe₂ superlattices with an adjustable bandgap and WSe₂ layer spacing are obtained. Both experimental results and theoretical calculations are used to demonstrate that such composites can accelerate the Li⁺ transport during Li–S reaction, improve the electrical conductivity, and optimize the Li–S redox catalysis reaction. Moreover, dual LiPS adsorption sites at the superlattice interface effectively inhibit the shuttle effect and boost the cycling stability.

2. Results and Discussion

2D NG/WSe₂ superlattices were produced in two steps, as schematized in **Scheme 1**. The first step involves the solvothermal reaction of ammonium metatungstate (AMT) and selenium powder in the presence of PVP. In the second step, the obtained powder is annealed at 800 °C within an inert atmosphere.

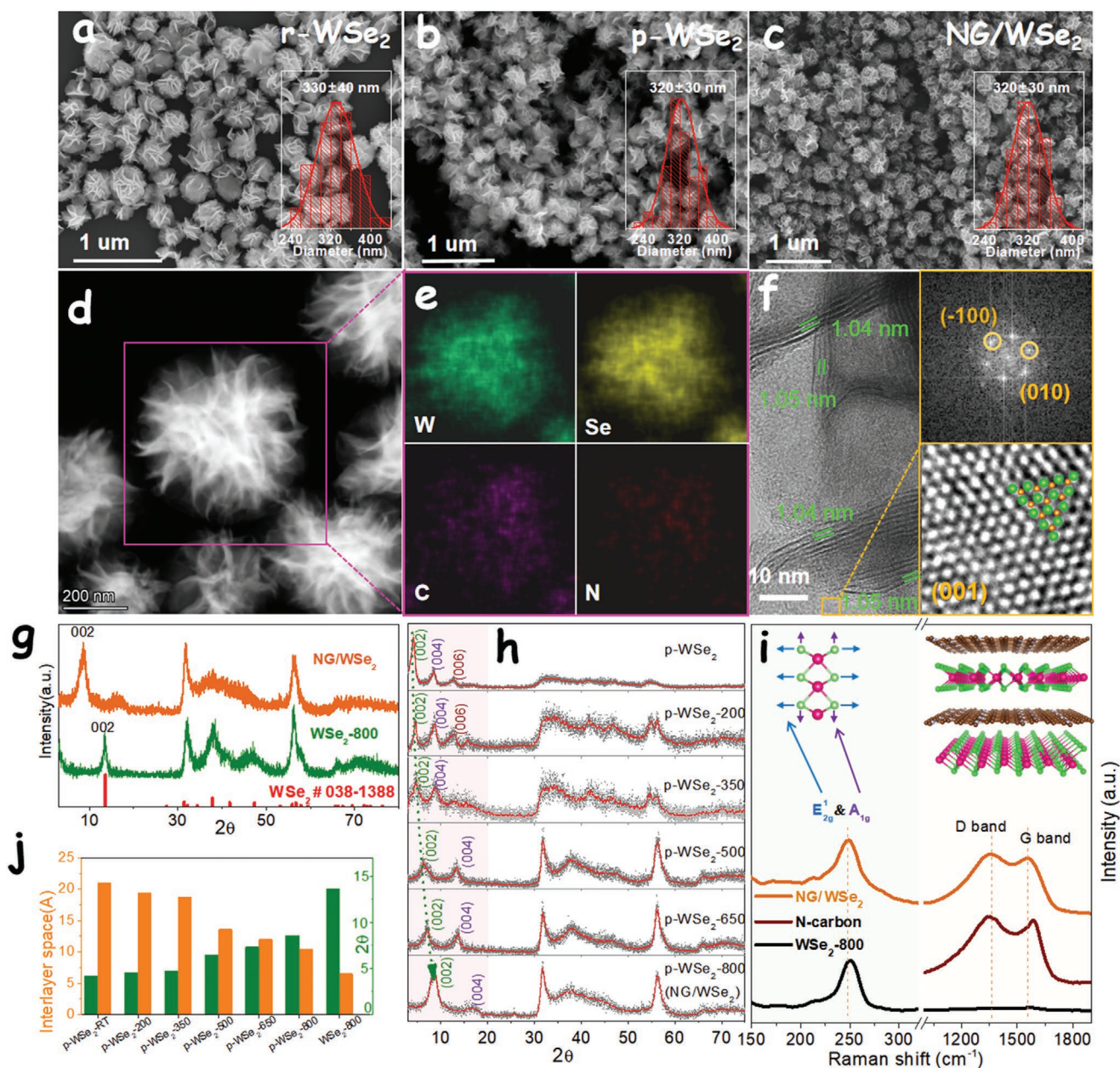


Figure 1. a–c) SEM images of r-WSe₂ (a), p-WSe₂ (b), and NG/WSe₂ (c). Inset histograms show the particle diameter distributions. d) HADDF-STEM image of NG/WSe₂ superlattice and e) EDX element maps. f) HRTEM image of an NG/WSe₂ superlattice with FFT spectrum and enlarged image of the yellow frame. g) XRD patterns of WSe₂-800 and NG/WSe₂ samples. h) XRD patterns of p-WSe₂ annealed at different temperatures. j) (002) XRD peak position and the corresponding interlayer space calculated from Bragg's law. i) Raman spectra of N-carbon, WSe₂-800, and NG/WSe₂ samples.

Figure 1a and Figure S1a, Supporting Information, display scanning electron microscopy (SEM) and high-angle annular dark-field scanning transmission electron microscopy (HADDF-STEM) images of the product obtained when no PVP was added to the reaction mixture. Without PVP, the obtained product, named raw-WSe₂ (r-WSe₂), was composed of nanosheet-based 330 ± 40 nm quasi-spherical particles. Energy-dispersive X-ray spectroscopy (EDS) analysis of the r-WSe₂ particles showed a W:Se atomic ratio of 1:2.1 (Figure S1b, Supporting Information). The small Se excess was related to residual Se from the synthesis process, and it could be removed in the subsequent annealing step.

When the solvothermal reaction was carried out in the presence of PVP, the obtained product was referred to as PVP-WSe₂ (p-WSe₂). The morphology of the p-WSe₂ particles was similar to that of r-WSe₂, with an average particle size of 320 ± 30 nm (Figure 1b). EDS mapping analysis showed a uniform distribution of C, N, O, W, and Se, with a W:Se atomic ratio of 1:2.3 (Figure S2a, Supporting Information). Fourier transform infrared spectroscopy analysis displayed the absorption fingerprints of the –C–N and carbonyl groups of PVP at 1650 and 1286 cm⁻¹, respectively,^[27] demonstrating the formation of a hybrid PVP-WSe₂ organic-inorganic composite (Figure S2b, Supporting Information).

The thermogravimetric analysis (TGA) of p-WSe₂ showed a weight profile similar to that of PVP (Figure S2c, Supporting Information), confirming the presence of PVP molecules or their derivatives within the p-WSe₂ composite. The minor weight loss below 300 °C is associated with the removal of water or small organic molecule (e.g., DMF) and residual Se. The more drastic weight loss at 350–450 °C is related to the decomposition and carbonation of the PVP molecular chains. The moderate mass loss at higher temperatures, in the range of 450–800 °C, is associated with a further graphitization process that enhances crystallinity.^[28]

In the second step, the p-WSe₂ was annealed at 800 °C in an inert atmosphere to decompose interlaminar PVP into N-doped graphitic carbon.^[29] As observed by SEM, the annealed material, named NG/WSe₂, displayed a similar morphology to that of r-WSe₂ and p-WSe₂, with 320 ± 30 nm quasi-spherical particles made of nanosheets (Figure 1c). HADDF-STEM micrographs and EDS elemental maps more clearly displayed the nanosheet-based structure of the spherical particles and their uniform W, Se, C, and N composition (Figure 1d,e, and Figure S3, Supporting Information). High-resolution transmission electron microscope (HRTEM) images displayed the NG/WSe₂ (002) interlayer spacing to be 1.04 nm (Figure 1f), well above the 0.65 nm measured from r-WSe₂ annealed at the same temperature (WSe₂-800, Scheme 1 and Figure S4a, Supporting Information) and approximately equal to the sum of the layer spacings of graphite carbon (0.34 nm) and WSe₂ (0.65 nm). The enlarged HRTEM image of the NG/WSe₂ nanosheets and the related FFT diffraction pattern displays an atomic W distribution that is consistent with hexagonal WSe₂ belonging to the p63/mmc space group, as it corresponds to the 2H phase of WSe₂ (Figure 1f inset). While the large atomic number difference between W and C did not allow observing the isolated graphite layers within the WSe₂ layered structure, we hypothesize that the enlarged interlayer space is related to the presence of graphitic carbon in the WSe₂ interlayers.

The X-ray diffraction (XRD) pattern of WSe₂-800 (Figure 1g) showed stronger diffraction peaks at 13.6°, 31.4°, 37.8°, and 55.9° than the precursor r-WSe₂ (Figure S1c, Supporting Information), which were indexed with the (002), (100), (103), and (110) planes of WSe₂ (JCPDS No. 038-1388).^[30] Most XRD peaks of NG/WSe₂ coincided with those of WSe₂-800, except for the (002) family planes, which was significantly shifted from 13.6° to 8.5°. This shift revealed an interlayer distance increase from 6.5 to 10.4 Å, which matches well with the results obtained by HRTEM (Figure 1f and Figure S4a, Supporting Information). We further simulated the XRD pattern of an NG/WSe₂ superlattice configuration (details can be found in the Supporting Information). As shown in Figure S5, Supporting Information, the two peaks at 8.5° and 17.0° in the experimental XRD pattern of NG/WSe₂ (Figure 1g) match well with the simulated (002) and (004) diffraction peaks of the superlattice.^[10,31] Interestingly, we investigated the 2H stacking and 3R stacking configuration of transition metal dichalcogenides in the superlattice structure. The best fit was obtained considering the 2H stacking. Thus, simulation results point towards the NG/WSe₂ superlattice maintaining the inversion symmetry of the original WSe₂ crystal.^[32]

On the other hand, the adjustment of the calcination temperature enabled us to control the interlayer spacing in an unprecedented wide range. According to XRD results, the (002) diffraction peak located at 4.2°, 4.5°, 4.7°, 6.5°, 7.3°, 8.5° as the calcination temperature increased from room temperature (RT) to 200, 350, 500, 650, and 800 °C, and thus the interlayer spacing of p-WSe₂ decreased from 21 to 19.4, 18.7, 13.6, 12, and 10.4 Å, respectively (Figure 1h,j). In addition to the strongest second-order diffraction peak (002) at 4.2°, p-WSe₂ clearly showed a series of higher-order diffraction peaks, (004) and (006), as labeled in Figure 1h and simulated in Figure S6, Supporting Information (see details in the Supporting Information). To the best of our knowledge, this is the widest continuous adjustable range of interlayer spacing reported for a 2D material, which opens the door to a wide range of applications not only in the field of rechargeable batteries but also in other fields like ionic sieves.^[7]

As obtained with the four-point probe method, the NG/WSe₂ superlattices annealed at 800 °C displayed a high electrical conductivity, up to 6.47 S cm⁻¹, which was two orders of magnitude above that of WSe₂-800 (Figure S7, Supporting Information). As expected, the electrical conductivity significantly increased with the calcination temperature. The high electrical conductivity of the NG/WSe₂ samples is consistent with the graphitization of the WSe₂ interlayer polymer and it is critical for the effective use of the composite material as sulfur host in LSB cathodes.^[15]

Figure 1i shows the Raman spectra of NG/WSe₂ and WSe₂-800 samples. A peak at ≈250 cm⁻¹ was observed in the two samples and it was attributed to the E_{1g} and A_{1g} modes of the WSe₂ 2H phase, which correspond to the axial and lateral stretching, respectively.^[33] The presence of interlayer product slightly affects the axial and lateral stretching of the WSe₂ layer, resulting in a minor shift of the peak, from 249 to 251 cm⁻¹.^[34,35] Meanwhile, NG/WSe₂ displayed two additional peaks at around 1358 and 1560 cm⁻¹ that were assigned to the D band (disordered carbon) and G band (sp²-hybridized graphitic carbon) of carbon materials, respectively.^[35,36] Compared with the graphitic N-doped carbon obtained by calcination of PVP (N-carbon, Figure S8, Supporting Information, see details in the experimental section and the Supporting Information), the shift of the G band in the Raman spectrum of NG/WSe₂ reflects that the interlayer NG was significantly affected by the sandwiched WSe₂ layer. The intensity ratio of the two peaks (I_D/I_G) in the NG/WSe₂ spectrum was estimated at 1.08 (close to the value of N-carbon, 1.05), indicating a defective carbon structure that we associated with the formation of N-doped carbon.^[37]

Notice that while the fingerprint of carbon was clearly observed in the Raman spectrum of NG/WSe₂, no carbon/graphite-related XRD peaks were obtained, and no graphene layer could be identified by extensive HRTEM characterization, which is consistent with graphene layers intercalated within the WSe₂ structure to form an NG/WSe₂ superlattice, as illustrated in Figure 1i.

Overall, the above data demonstrate the formation of a high electrical conductivity NG/WSe₂ superlattice with a tunable WSe₂ interlayer distance by a simple (only 2 steps) and easily scalable procedure that provided a high material yield of ≈85% (a detailed comparison can be found in Figure S9, Supporting Information). These composites were obtained using PVP

as a structure-directing agent. We speculate that in DMF solvent PVP couples with the (001) surface of the nucleating WSe₂, inhibiting continuous growth in the [001] direction but promoting a stable 2D growth of WSe₂ monolayer. As the reaction progresses, PVP forms a coating layer on the surface of WSe₂. The other side of the PVP molecules bind to the WSe₂ monolayer are used as heterogeneous nucleation sites for the growth of an additional WSe₂ nanosheet. This layer-by-layer growth results in the formation of -WSe₂-PVP-WSe₂-PVP-superlattice nanosheets. The presence of the PVP molecular layer effectively separates the WSe₂ stack, shifting the (002) peak/spot in the XRD and electron diffraction patterns.^[38,39]

A priori, the same procedure should allow obtaining hybrid organic-inorganic composites that contain other organic molecules/polymers that have some affinity for the surface of metal dichalcogenide nanostructures. To test this hypothesis, PVP was replaced by other organics/surfactants commonly used to direct the synthesis of dichalcogenide nanoparticles, such as cetyltrimethylammonium bromide (CTAB), pluronic (F127), sodium dodecyl sulfate (SDS), and glucose (GLU). Figure S10, Supporting Information, shows SEM images and XRD patterns of the obtained materials. As observed by SEM, all the obtained materials showed a nanosheet-based morphology, similar to that of p-WSe₂. Besides, XRD analysis showed the product obtained from the solvothermal reaction to display the charac-

teristic XRD peaks of WSe₂ with a clear shift of the (002) interlayer spacing, confirming the successful intercalation of the organic within the WSe₂ layered structure. However, this shift of the (002) XRD peak disappeared after the calcination treatment. Thus, none of these alternative organics could be stably pyrolyzed into interlayer graphene at high temperatures to yield the NG/WSe₂ superlattice material. We hypothesize that the successful use of PVP is related to its robust molecular chain structure and its high intercalation content, which guarantee the graphitization transformation during the pyrolysis process rather than its volatilization from the interlayer.

The electronic band structure and the associated density of state (DOS) of NG, WSe₂, and NG/WSe₂ were determined using density functional theory (DFT). As expected, NG exhibited a typical conductor band structure and DOS, with the Fermi level lying within a continuous band of states (Figure 2a). On the other hand, WSe₂ displayed a semiconductor structure with a bandgap of 1.68 eV (Figure 2b).^[40] The combination of both within the NG/WSe₂ superlattice showed no gap of states at the Fermi level (Figure 2c), which is consistent with a metallic character and the high electrical conductivity measured by the four-probe method.

X-ray photoelectron spectroscopy (XPS) analysis was used to experimentally corroborate the Fermi level position and study the chemical state of the different elements. As observed in

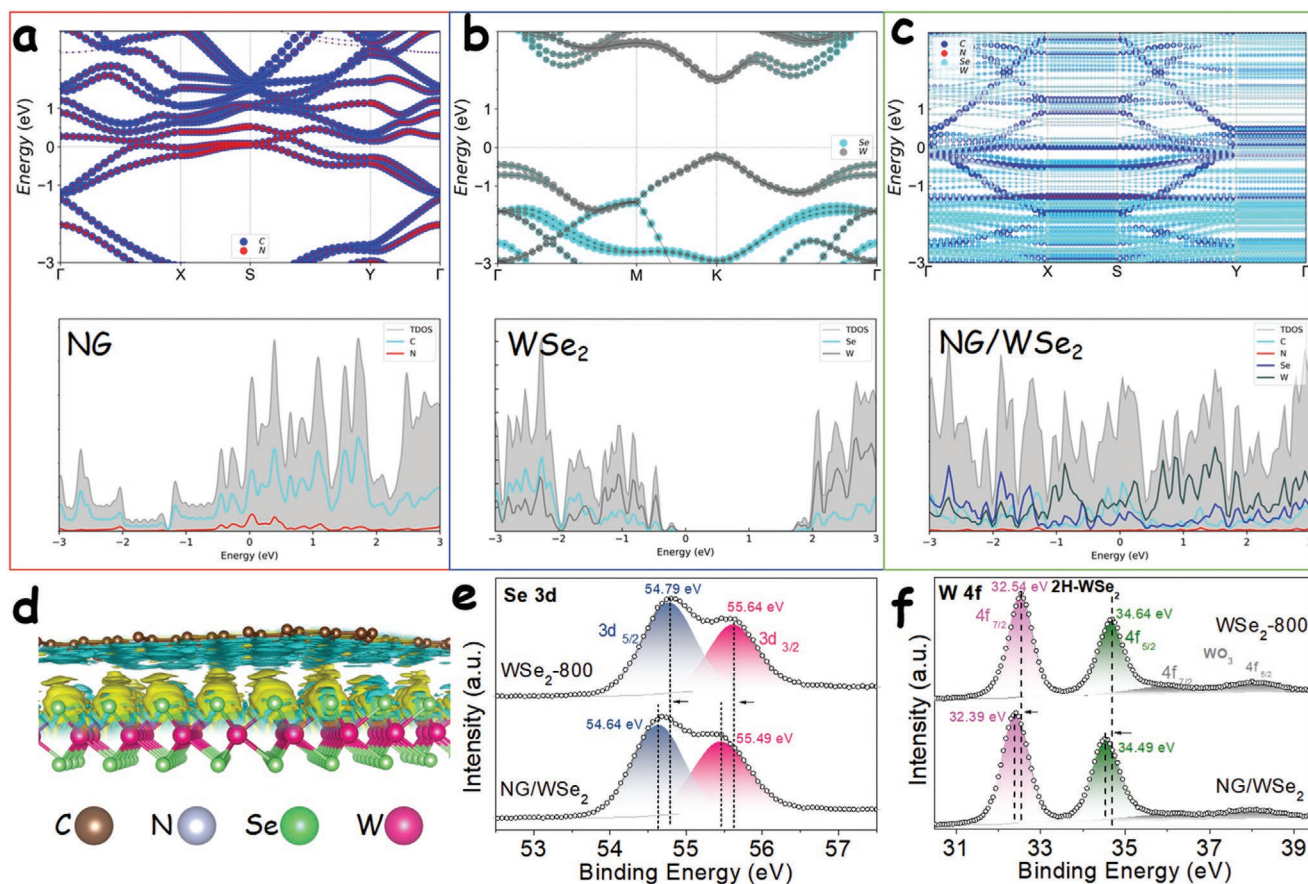


Figure 2. a–c) HSE06 band structure and DOSs of NG (a), WSe₂ (b), and NG/WSe₂ superlattice (c). d) Charge density differential plot of the NG/WSe₂ superlattice. The yellow and blue regions represent increased and decreased electron density, respectively. e) Se 3d and f) W 4f high-resolution XPS spectra from WSe₂-800 and NG/WSe₂ samples.

Figure S11a, Supporting Information, the Fermi level of the NG/WSe₂ superlattice at ambient temperature is located within a band of states, delimiting the occupied and unoccupied states, consistent with DFT calculations. The high-resolution Se 3d XPS spectrum of WSe₂-800 and the NG/WSe₂ composite displayed one doublet associated with Se²⁻ anions within a WSe₂ chemical environment (Figure 2e).^[24] This Se 3d doublet was located at 55.64 eV (Se 3d_{3/2}) and 54.79 eV (3d_{5/2}) for WSe₂-800, but it was slightly shifted (≈0.15 eV) to lower binding energies in NG/WSe₂. The high-resolution W 4f XPS spectra of WSe₂-800 and NG/WSe₂ were also fitted with one doublet, associated with W⁴⁺ within a WSe₂ environment (Figure 2f).^[24] The W 4f XPS spectrum of NG/WSe₂ was also red-shifted ≈0.15 eV with respect to that of WSe₂-800. We hypothesize that the coincident redshift of the binding energies of both anions and cations within WSe₂ was related to a transfer of charge between NG and WSe₂ layers.

DFT calculations of the 3D charge density difference at the NG/WSe₂ heterojunction were employed to analyze the charge transfer between NG and WSe₂ layers. Calculations demonstrated a reduction of the electron density in the NG layer, as shown by the blue areas in Figure 2d, and an accumulation of the electron density in the WSe₂ layer, as represented by the yellow areas. The accumulation of negative charge in the WSe₂ layer facilitates the extraction of electrons from the W and Se levels, as observed by XPS analysis. Thus, experimental and computational evidence demonstrate that the charge transfer occurs at the atomic interface between the two materials, with the negative charge being transferred from the NG layer to the WSe₂ layer. A Bader analysis quantified the charge transfer in 0.038 electrons per supercell. This differential accumulation of charge is associated with a built-in electric field that can promote the adsorption of LiPS, which is crucial for inhibiting the shuttle effect and improving the cycle performance of LSBs.^[21,41,42,43]

The LiPS-adsorption ability of NG/WSe₂ was experimentally compared with that of WSe₂-800 and graphene (G) by immersing 20 mg of each material in 5 mM Li₂S₄ solutions overnight and observing their color change. As observed from the optical images in Figure 3a, the original 5 mM Li₂S₄ solution had an orange color. In the presence of graphene, the color of the solution remained unchanged, as expected from the very low LiPS adsorption ability of the nonpolar graphene surface. The solution containing WSe₂-800 became more pallid, consistent with the WSe₂ ability to chemisorb LiPS. But the solution containing NG/WSe₂ was completely decolorized, demonstrating the much stronger affinity of this material towards Li₂S₄ adsorption. This stronger affinity could be in part related to the built-in electric field between NG and WSe₂. The adsorption ability could be quantified by analyzing the supernatant using UV-vis spectroscopy (Figure 3b). Li₂S₄ presents a strong absorption band in the range of 400–500 nm.^[43] The absorbance in this region strongly decreased in the presence of WSe₂ and especially NG/WSe₂, indicating that most of the Li₂S₄ in the solution had been captured by the adsorber.

The NG/WSe₂ chemical states after the Li₂S₄ adsorption test were analyzed by XPS. From the comparison of the N 1s spectra of the superlattices before and after Li₂S₄ adsorption (Figure 3c), a shift of the pyridinic-N band from 399.89 eV to 399.74 eV

and of the graphite-N band from 401.04 eV to 400.89 eV, was observed.^[44] This shift of the N 1s electronic states toward lower binding energies is related to a decrease of the chemical environment electronegativity that we associate with the interaction of N with Li-ions. Besides, a small N 1s band at 397.74 eV was observed in the XPS spectrum of the material after Li₂S₄ adsorption. This additional band was attributed to the N-Li bond formation during the adsorption process. The strong influence of the Li₂S₄ adsorption process on the N 1s XPS spectra is related to the anchoring of the Lewis acid Li atoms of LiPS on Lewis base nitrogen sites through dipole-dipole interactions.^[20,45] On the other hand, after the Li₂S₄ adsorption test, the high-resolution W 4f XPS spectrum shifted in the opposite direction than N 1s, that is, towards higher binding energies (Figure 3d). This shift is related to an increase of the chemical environment electronegativity, which is associated with the interaction of W in the WSe₂ lattice with S atoms in LiPS.

DFT calculations were used to further investigate the adsorption of LiPS at WSe₂ and NG/WSe₂ sites. According to previous reports, in 2D transition metal dichalcogenides, LiPS preferentially adsorb at edge-exposed metal sites sandwiched between two chalcogen layers.^[17,22,46] Thus, we focused on the calculation of the binding energy (Eb) and adsorption configuration of different LiPS molecules adsorbed on the edge sites of WSe₂ and NG/WSe₂. Figure S12, Supporting Information, displays the optimized geometric configuration of WSe₂-LiPS species with five different lithiation levels (Li₂S₈, Li₂S₆, Li₂S₄, Li₂S₂, Li₂S). The WSe₂-Li₂S₄ adsorption configuration employed W-S bonds to immobilize the soluble Li₂S₄ species with an Eb of -1.15 eV (Figure 3e), which is higher (in absolute value) than the Eb reported for graphene (< -1 eV).^[47,48] This higher absolute value of Eb correlates well with the experimental data on Li₂S₄ adsorption discussed above. A much higher absolute value of Eb was obtained for the NG/WSe₂-Li₂S₄ adsorption, -9.75 eV. This very high absolute value of Eb is related to the adsorption of LiPS at two sites, as shown in the optimized geometric configuration displayed in Figure 3f. This optimized configuration consisted of a Li₂S₄ anchored by Li-N and W-S bonds on the NG-WSe₂ surface. Besides, DFT calculations showed the W-S bond within the NG/WSe₂-Li₂S₄ system to be shorter than within WSe₂-Li₂S₄, while the distance of the Li-S bond within the LiPS increases when Li₂S₄ is adsorbed on NG/WSe₂ instead of WSe₂ (Figure 3g). The optimized configurations and Eb of NG/WSe₂-LiPS at other lithiation stages are illustrated in Figure S13, Supporting Information and Figure 3f, respectively. Overall, the DFT results demonstrated that the NG-WSe₂ superlattice can employ dual-adsorption sites in sublattice layers to deliver robust LiPS chemisorption, which is consistent with experimental results from the XPS analysis and adsorption test. The combination of DFT calculations and experimental data demonstrate that NG/WSe₂ contains very effective lithiophilic/sulfurophilic adsorption sites able to trap polysulfides, which should allow minimizing the shuttle effect and enable a uniform deposition of the sulfur-based reaction products.

Sulfur was loaded within the porous structure of the host materials by a melting method (see details in the experimental section), to obtain S@NG/WSe₂, S@WSe₂-800, and S@G. After S loading, the specific surface area of NG/WSe₂ decreased from 59.6 to 0.86 m² g⁻¹ (Figure S14a, Supporting Information).

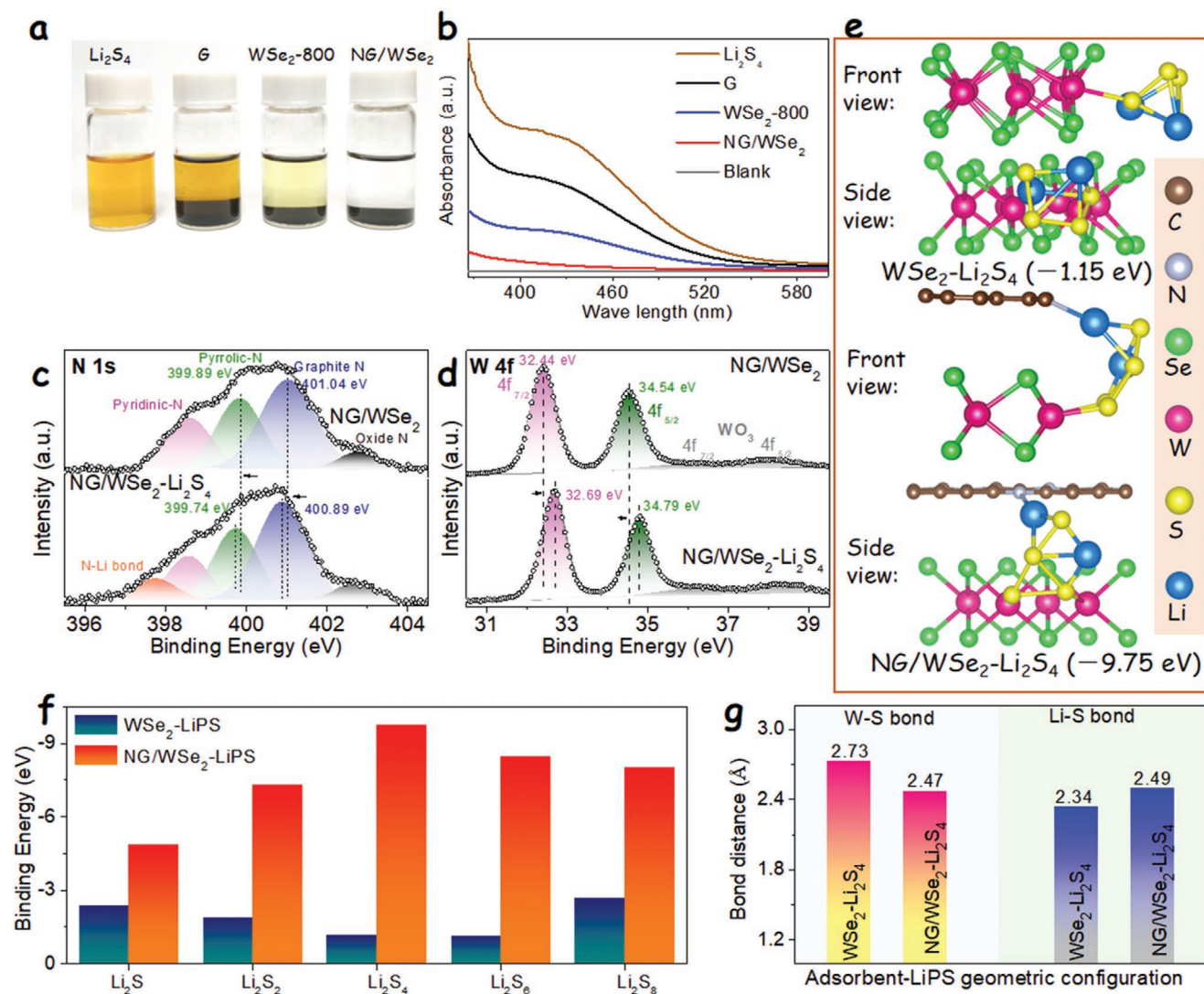


Figure 3. a) Optical photograph and b) UV-vis spectra of Li_2S_4 solutions containing the different adsorbents overnight. c) N 1s and d) W 4f XPS spectra of NG/ WSe_2 before and after Li_2S_4 . e) Relaxed Li_2S_4 -adsorbed configurations on the edge of WSe_2 and NG/ WSe_2 . f) Binding energies between LiPS (Li_2S , Li_2S_2 , Li_2S_4 , Li_2S_6 , and Li_2S_8) and WSe_2 and NG/ WSe_2 . g) W-S bond and Li-S bond distances in $\text{WSe}_2\text{-Li}_2\text{S}_4$ and NG/ $\text{WSe}_2\text{-Li}_2\text{S}_4$ configurations. The Li-S bond distance is selected as the closest distance to the adsorbent structure.

XRD patterns of the S-loaded host clearly showed the diffraction peaks associated with the cubic sulfur phase (JCPDS No. 08-0247, Figure S14b, Supporting Information), together with the (002) peak of NG/ WSe_2 . TGA allowed quantifying the sulfur content within S@NG/ WSe_2 in a 73.8 wt% (Figure S14c, Supporting Information). Besides, SEM and EDX elemental maps showed a uniform distribution of sulfur within S@NG/ WSe_2 . Similar results were obtained from the reference samples, S@ WSe_2 -800 and S@G, which contained 73.2–73.4 wt% of S, as displayed in Figure S15, Supporting Information.

The sulfur cathodes were assembled into coin cells to evaluate their electrochemical performance. Figure 4a displays the galvanostatic charge/discharge curves of the three electrodes, S@NG/ WSe_2 , S@ WSe_2 -800, and S@G, at a 0.1 C current rate. All the tested electrodes showed one charging and two discharging plateaus, associated with the relatively complex sulfur redox reaction. The two discharge plateaus reflect

the 4-electron reduction of sulfur to soluble long-chain LiPS ($\text{S}_8 + 4\text{Li}^+ + 4\text{e}^- \rightarrow 2\text{Li}_2\text{S}_4$) and the subsequent 12-electron reaction to insoluble lithium sulfide ($2\text{Li}_2\text{S}_4 + 12\text{Li}^+ + 12\text{e}^- \rightarrow 8\text{Li}_2\text{S}$). The anodic plateau obtained during the charging process is attributed to a reverse multi-step sulfur oxidation process in which short-chain sulfides are converted to LiPS and eventually to sulfur.^[49] The S@NG/ WSe_2 electrode showed a significantly higher discharge capacity (up to 1513 mAh g^{-1}) than S@ WSe_2 -800 (1239 mAh g^{-1}) and S@G (995 mAh g^{-1}) electrodes. This capacity was contributed mainly by sulfur, since the sulfur-free NG/ WSe_2 electrode showed a very low capacity to store lithium ions within the voltage range 1.7–2.8 V, as displayed in Figure S16, Supporting Information.

The voltage gap between the oxidation platform and the second reduction platform at 50% discharge capacity, ΔE , is considered as the polarization potential in the Li-S reaction, which is a measure of the LiPS transformation kinetics.^[43] The

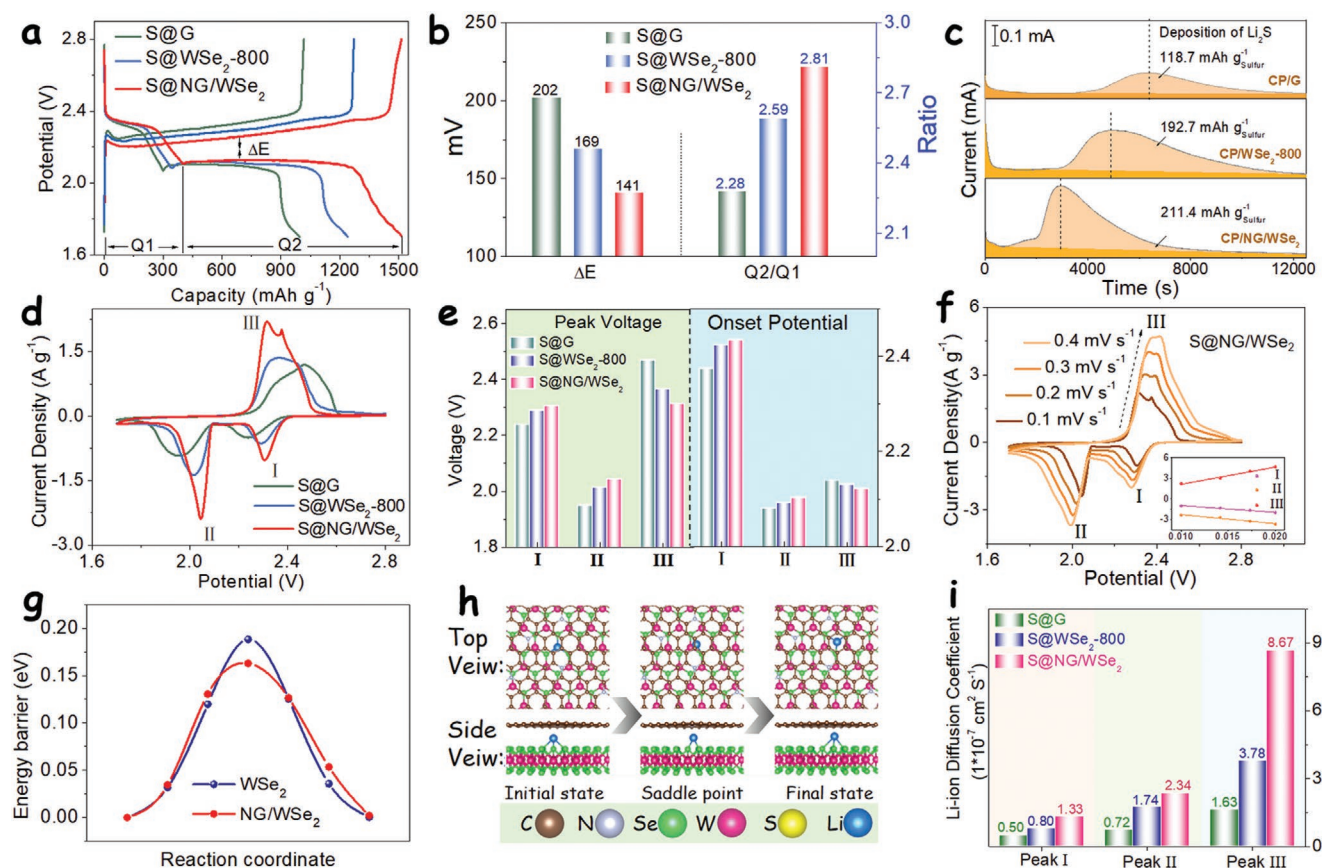


Figure 4. a) Charge/discharge curves of different electrodes at 0.1 C current rate. b) ΔE and Q2/Q1 values obtained from charge/discharge curves. c) Potentiostatic discharge profile of Li_2S nucleation at 2.05 V on different electrodes with Li_2S_8 catholyte. d) CV profiles of lithium-sulfur coin cells with different electrodes. (e) Peak voltages and onset potentials obtained from CV curves of the S@NG/WSe₂ electrode at various scan rates. Inset shows the CV peak current density (A g^{-1}) for peaks I, II, and III versus the square root of the scan rate (V s^{-1}). The oxidation peak current is selected as the highest current point in CV curves. g) Energy profiles of Li ion migration in the interlayer of NG/WSe₂. h) Illustration of stages of Li ion diffusing in the interlayer of NG/WSe₂. i) Li-ion diffusion coefficient value at CV peaks I, II, and III.

polarization potential obtained with the S@NG/WSe₂ electrode ($\Delta E = 141$ mV) was significantly lower than that obtained with S@WSe₂-800 ($\Delta E = 169$ mV) and S@G ($\Delta E = 202$ mV). Besides, the overpotentials obtained with the S@NG/WSe₂ electrode, associated with the phase transition between soluble Li_2S_4 and insoluble $\text{Li}_2\text{S}_2/\text{Li}_2\text{S}$,^[46] were much lower than those obtained with the S@WSe₂-800 and S@G electrodes (Figure S17, Supporting Information).

The ratio of the capacities of the first (Q1) and second (Q2) discharge plateaus can be used as an additional quantitative measure of the catalytic activity of the host materials toward the LiPS conversion reaction.^[20] As the first discharge plateau involves 4 electrons and the second one involves 12 electrons, the theoretical Q2/Q1 ratio is 3. However, in practice, this ratio is significantly reduced because of an incomplete sulfur reduction to a combination of Li_2S and Li_2S_2 instead of pure Li_2S . This incomplete reduction is the result of the slow reaction kinetics of the liquid to solid transition. Besides, the Q2/Q1 ratio is also reduced because part of the soluble LiPS is lost during the second plateau (Q2). Therefore, the Q2/Q1 ratio provides a measure of the degree of completion of the reduction reaction, associated with the host catalytic ability, and the inhibition of the shuttle effect. Figure 4b displays the Q2/Q1 ratios

of the three host materials. The S@NG/WSe₂ electrode showed the highest Q2/Q1 ratio at 2.81, close to the theoretical value and well above that of S@WSe₂-800 (2.59) and S@G (2.28).

The final reaction step, the conversion of Li_2S_2 to Li_2S ($4\text{Li}_2\text{S}_2 + 8\text{Li}^+ + 8\text{e}^- \rightarrow 8\text{Li}_2\text{S}$) accounts for 50% of the capacity associated with the Li-S reaction. This step is at the same time the one with the more sluggish reaction kinetics and thus the most demanding for the catalytic material. Thus, Li_2S nucleation tests were used to quantitatively evaluate the impact of host materials in this transformation process.^[50] As can be seen from the potentiostatic discharge curves in Figure 4c, the NG/WSe₂-based electrode obtained by loading NG/WSe₂ on carbon paper (CP/NG/WSe₂) showed the sharpest nucleation peak and the fastest Li_2S nucleation response when compared with CP/WSe₂-800 and CP/G electrodes. According to Faraday's Law, by integrating the area of the current-time curve a nucleation capacity of 211.4 mAh g^{-1} was obtained for the CP/NG/WSe₂, well above that CP/WSe₂-800 (192.7 mAh g^{-1}) and CP/G (118.7 mAh g^{-1}). The cathode surface morphology after the nucleation test was studied by SEM (Figure S18, Supporting Information). The SEM image of CP/NG/WSe₂ electrode obtained from the disassembled cell showed a more uniform and denser Li_2S layer than the CP/WSe₂-800 electrode, which

further demonstrated that NG/WSe₂ could significantly boost the Li₂S nucleation process.

Overall, the above data demonstrate that the NG/WSe₂-based electrode can effectively reduce the Li–S redox reaction overpotential, minimize the LiPS shuttle effect and promote the nucleation reaction of Li₂S.

Figure 4d shows the cyclic voltammetry (CV) curves obtained from S@NG/WSe₂, S@WSe₂-800, and S@G electrodes. All curves display two cathodic peaks (peaks I and II) and one anodic peak (peak III), which is consistent with the measured charge/discharge plateaus. Also consistent with the above results, among the three tested electrodes, S@NG/WSe₂ showed the highest peak current densities and the most positive/negative potential of the cathode/anode peaks (Figure 4e). The S@NG/WSe₂ electrode also displayed the highest/lowest reduction/oxidation onset potentials at a current density of 10 μA cm⁻² (Figure S19, Supporting Information).^[50,51] Thus, CV curves further evidenced NG/WSe₂ to be the most effective electrocatalyst to promote the kinetics of polysulfide redox reaction.

Besides electron transport/transfer properties and catalytic activity, the reactant diffusivity is an additional key parameter determining the dynamics of an electrochemical reaction.^[52] In the particular case of LSBs, the low electrical conductivity of S₈, polysulfides, and Li₂S demands for very effective and rapid diffusion of Li⁺ within the sulfur host.^[53] DFT calculations were used to determine the Li-ion diffusion pathways and diffusion barriers in the interlayer space of WSe₂ and NG/WSe₂ (Figure 4g,h, and Figure S20, Supporting Information). Both materials present effective channels for Li⁺ diffusion with a low energy barrier. However, the presence of NG within the WSe₂ interlayer in NG/WSe₂ allowed reducing the energy barrier for Li⁺ diffusion from 0.188 to 0.163 eV, thus pointing towards a faster Li-ion diffusion capability and stronger interfacial ions transfer dynamics.^[54,55]

The Li⁺ ion diffusivity was experimentally determined by measuring CV curves at different scan rates (0.1 to 0.4 mV s⁻¹). As observed in Figure 4f and Figure S21, Supporting Information, for all the electrodes, when increasing the scan rate, the reduction (oxidation) peaks shifted towards lower (higher) potentials, the peak current density increased and the polarization voltage (voltage gap between peak I and peak III) augmented. Among the different electrodes, S@NG/WSe₂ showed the highest current densities and the lowest polarization voltage at all scanning rates, indicating the fastest LiPS conversion kinetics. Besides, a linear relationship was observed between the peak current and the square root of the scanning rate for the three peaks, which denotes diffusion-controlled reduction and oxidation reactions (inset of Figure 4f). Thus, the Randles-Sevcik equation was applied to calculate the Li⁺ diffusion coefficient in the process:^[43,56]

$$I_p = (2.69 \times 10^5) n^{1.5} A D_{Li^+}^{0.5} C_{Li^+} \nu^{0.5} \quad (1)$$

where I_p is the peak current (A), n is the number of charge transfer, A is the geometric electrode area (cm²), D_{Li^+} is the Li⁺ diffusion coefficient, C_{Li^+} is the concentration of Li⁺ in the electrolyte (mol cm⁻³), and ν is the scan rate (V s⁻¹). Being n , A , and C_{Li^+} constants, a steeper $I_p/\nu^{0.5}$ slope indicates a faster Li⁺ diffusion. The S@NG/WSe₂ electrode was characterized by the

steepest slopes, involving the highest Li⁺ diffusivities during the Li–S redox reaction.^[20] Quantitatively, the D_{Li^+} calculated from peaks I, II, and III were 1.3, 2.3, and 8.7×10^{-7} cm² s⁻¹, respectively (Figure 4i). The Li⁺ diffusion rate is influenced by the electrode structure, that is, the density and effectiveness of the Li⁺ transport channels, the electrolyte viscosity, which depends on the amount of dissolved LiPS, and the rate of formation/dissolution of the Li₂S/Li₂S₂ layer.^[57] The high Li⁺ diffusion rate of the S@NG/WSe₂ electrode is related to the large interlayer spacing promoting a rapid transport of Li ions within the host material and a promoted adsorption and catalytic conversion of LiPS that decrease the LiPS electrolyte concentration and accelerates the kinetics of Li₂S/Li₂S₂ formation/dissolution. This improved Li⁺ diffusivity should be reflected in a superior rate capability.

Rate performance tests were carried out in the current density range of 0.1 C to 5 C (Figure 5a). The S@NG/WSe₂ electrode showed the highest discharge capacities at all current rates, with an initial discharge capacity of 1597.5 mAh g⁻¹ at 0.1 C that indicates a high utilization of sulfur in the cathode. When the current was increased to 5 C, the S@NG/WSe₂ electrode still maintained a high average capacity of 569.5 mAh g⁻¹, well above that of S@WSe₂-800 (197.5 mAh g⁻¹) and S@G (9.2 mAh g⁻¹). Besides, S@NG/WSe₂ recovered an average capacity of 1131 mAh g⁻¹ when the current rate was returned to 0.2 C. Figure 5b displays the galvanostatic charge/discharge curves under different current rates. All discharge curves show two discharge plateaus, even at 5 C. In contrast, the S@WSe₂-800 cell showed a high increase of the polarization voltage and a reduced capacity in the charge/discharge profiles when increasing the current rate, and the S@G electrode was almost unable to release capacity at 5 C (Figure S22, Supporting Information).

Figure 5d displays 500 continuous cycles of the three different electrodes at 1 C. During cycling, the S@G electrode suffered a drastic capacity decay because of its lack of effective catalytic-adsorption sites, retaining just 34.4% (173 mAh g⁻¹) of its initial capacity after 500 cycles. In contrast, the S@WSe₂-800 electrode provided a larger initial capacity, 839 mAh g⁻¹, and it was able to retain 54.0% of it (453.3 mAh g⁻¹) after 500 cycles. But best results were obtained with the S@NG/WSe₂ electrode, which provided an initial discharge capacity at 1 C of 923 mAh g⁻¹, and it retained 81.3% of its capacity (750.4 mAh g⁻¹) after 500 cycles, which corresponds to a much lower capacity decay rate of just 0.037% per cycle.

Interestingly, we investigated the effect of other carbonaceous materials as intercalators on the electrochemical performance of the formed superlattice. Figure S23, Supporting Information, shows the results obtained using the GLU-WSe₂ superlattice (not annealed) as the sulfur host material. Indeed, the S@GLU-WSe₂ electrode was also characterized by a superior rate performance and cycle stability which can be in part related to the small amount of residual Se present in the unannealed material.^[58,59]

Figure 5c and Figure S24, Supporting Information, show the impedance changes of S@NG/WSe₂, S@WSe₂-800, and S@G electrodes before and after cycling at 1 C, and the equivalent circuits used to fit the data (inset in Figure 5c). The Nyquist plots of the electrochemical impedance spectroscopy (EIS) result

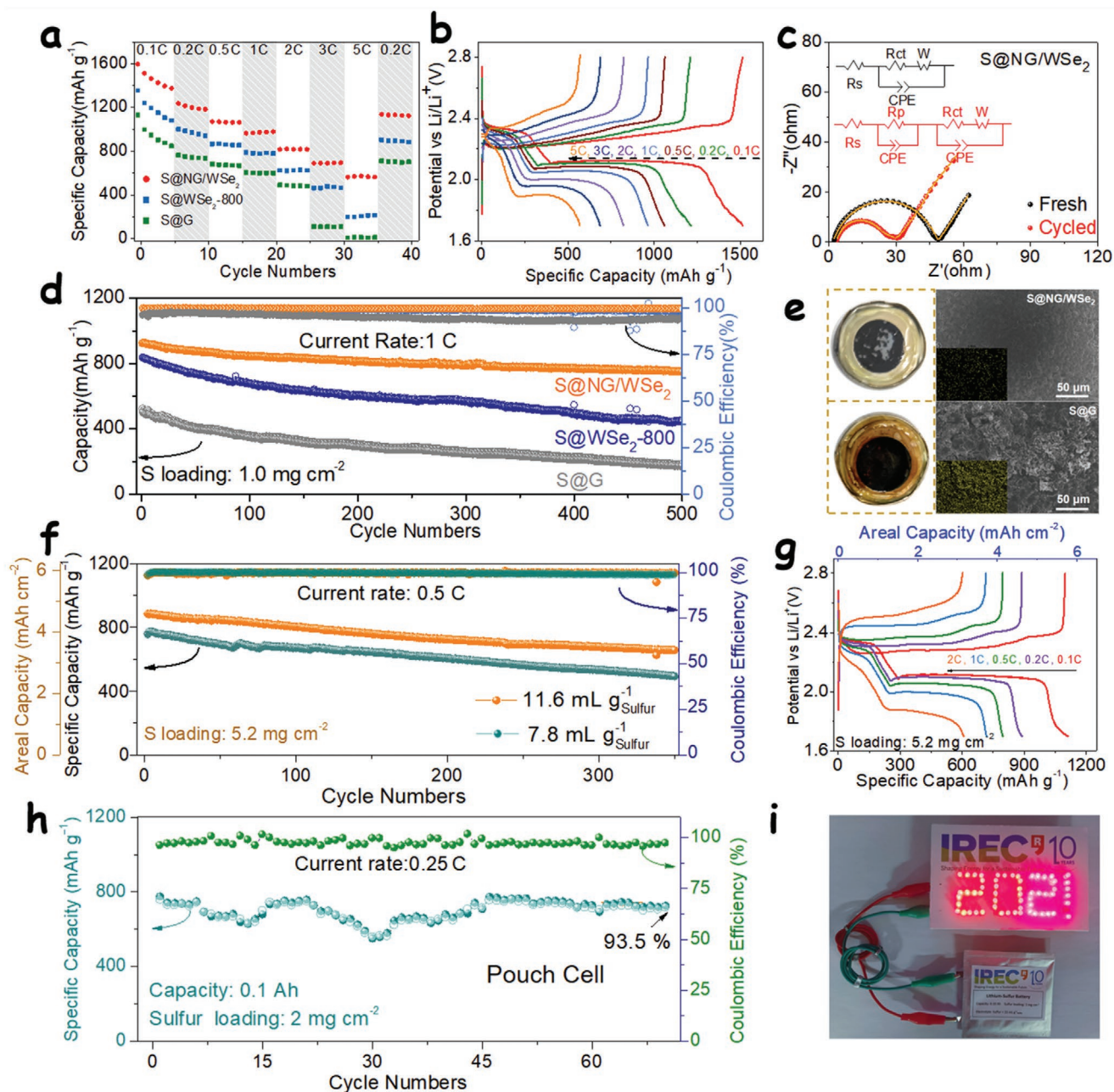


Figure 5. a) Rate performances of S@NG/WSe₂, S@WSe₂-800, and S@G electrodes. b) Charging/discharging curves of the S@NG/WSe₂ electrode at current rates from 0.1 to 5 C. c) Nyquist plot of the EIS results obtained from an S@NG/WSe₂ electrode before and after 100 cycles at 1 C. The Nyquist curves are fitted considering the equivalent circuits shown as inset, where R_s, R_p, R_{ct}, and W stand for the resistances of the electrolyte, the insoluble Li₂S₂/Li₂S precipitation layer, the interface charge-transport, and the semi-infinite Warburg diffusion, respectively; and CPE stands for the corresponding capacitances. d) Capacity retention of different electrodes at 1 C over 500 cycles. e) Optical images of membranes and SEM image of lithium foil recovered from cycled coin cells containing an S@NG/WSe₂ electrode (top) and an S@G electrode (down). The inset images show the map of the sulfur signal detected by EDX. f) Cycling stability of an S@NG/WSe₂ electrode with a high sulfur loading (5.2 mg cm⁻²) and a lower electrolyte usage (11.6 and 7.8 mL g⁻¹_{Sulfur}) at 0.5 C over 350 cycles. g) Charge/discharge curves of S@NG/WSe₂ electrodes with a 5.2 mg cm⁻² sulfur loading at various current rates. h) Cycling performances at 0.25 C of a pouch cell based on an S@NG/WSe₂ cathode. i) Optical photograph of a “2021” panel contained 58 red LEDs powered by a pouch cell based on an S@NG/WSe₂ electrode.

obtained from the fresh batteries show a semicircle at the high-frequency range related to the charge-transfer resistance (R_{ct}), and a sloping straight line at lower frequencies related to the lithium ions diffusion.^[60,61] The S@NG/WSe₂ fresh electrode showed the lowest R_{ct} (46.6 Ω) compared with S@WSe₂-800

(69.2 Ω) and S@G (77.9 Ω), which confirms the enhanced charge transferability of the superlattice cathode. After 100 cycles and keeping the cells in the charged state for the EIS test, all R_{ct} values were significantly reduced due to the activation of the process.^[20,43] Besides, the fitting of the Nyquist plots required a

new element to account for the additional semicircle appearing in the high-frequency range. This new feature is related to the impedance of the passivating layer in the cathode and anode created during the cycling (R_p in the equivalent circuit) and that was generated from the electrolyte decomposition.^[62,63] Li_2S corrosion in the anode surface caused by LiPS diffusion from cathode to anode,^[63] and residues of unoxidized $\text{Li}_2\text{S}/\text{Li}_2\text{S}_2$ in the cathode during the fast charge/discharge process.^[64,65] After cycling, the S@NG/WSe₂ electrode was characterized by the smallest resistances ($R_{ct} = 6.9 \Omega$ and $R_p = 19.5 \Omega$), well below that of cycled S@WSe₂-800 ($R_{ct} = 25.9 \Omega$ and $R_p = 40.4 \Omega$) and S@G ($R_{ct} = 75.2 \Omega$ and $R_p = 44.8 \Omega$). The small R_p values obtained with S/NG/WSe₂ suggest that NG/WSe₂ effectively inhibited the shuttle effect and promoted faster conversion kinetics of Li_2S , which effectively reduces the Li_2S corrosion in the anode and the residue of unoxidized $\text{Li}_2\text{S}/\text{Li}_2\text{S}_2$ in the cathode. The comparison of the slopes measured in the low-frequency range (Figure S24 d), confirmed the faster diffusion of Li^+ within the S@NG/WSe₂ electrode, which displayed the highest slopes both before and after cycling.

After 100 cycles, coin cells were disassembled to quantitatively assess the amount of LiPS diffusing to the anode material and the structural stability of the host material. After 100 cycles, the membranes of the NG/WSe₂ and S/NG cells showed a sharp color contrast (Figure 5e). The yellowish color of the membrane extracted from the S@NG/WSe₂ cell indicates a low LiPS diffusion and thus an effective capture of polysulfide species. In contrast, the dark brown color of the membrane obtained from the S@G cell indicated significant contamination with LiPS species not properly anchored to the cell cathode. Besides, the lithium anode of the cycled S@G coin cell displayed serious corrosion, multiple cracks, and notable contamination with sulfur (Figure 5e). In contrast, the lithium anode of the cycled S@NG/WSe₂ coin cell displayed a smooth and compact Li surface and low intensity of the EDS sulfur signal (Figure 5e), suggesting a negligible amount of LiPS reaching the anode.^[20,43] At the other side of the cell, despite the incorporation of conductive/binder additives and the grinding processes used for the slurry preparation, the nanosheet structure of NG/WSe₂ is still recognizable in the SEM image of the cycled S@NG/WSe₂ cathode (Figure S25, Supporting Information), indicating good mechanical stability of the superlattice during the lithiation/delithiation cycles.

The commercial application of high energy density LSBs requires maximizing the sulfur areal load and reducing the electrolyte volume. In this direction, we prepared S@NG/WSe₂ electrodes with a 5.2 mg cm^{-2} sulfur load and tested them within cells containing just $11.6 \text{ mL g}^{-1}_{\text{Sulfur}}$ of electrolyte. When cycled at a 0.5 C current rate, these cathodes achieved an initial discharge capacity of 885.3 mAh g^{-1} , which is equivalent to an areal capacity of 4.6 mAh cm^{-2} (Figure 5f), well above that of commercial lithium-ion batteries (4 mAh cm^{-2}). After 350 cycles, the discharge capacity remained at 656.0 mAh g^{-1} , which corresponds to a 74.1% capacity retention. Figure S26a, Supporting Information, displays the change of charge/discharge curves during the cycling process, exhibiting a steady decay process with the same charge/discharge plateaus. Figure 5g and Figure S26b, Supporting Information, display the rate performance of the high sulfur loading electrodes.

The S@NG/WSe₂ electrode containing 5.2 mg cm^{-2} of sulfur showed a high initial capacity of 1188 mAh g^{-1} at a current rate of 0.1 C. Even at a high current rate of 2 C, a stable discharge capacity of 607 mAh g^{-1} was achieved. Besides, the capacity recovered well when the current rate was reduced back to 0.2 C. The charge/discharge curves at all different current rates clearly show one charging plateau and two discharge plateaus (Figure 5g), demonstrating that even at high sulfur loadings, the NG/WSe₂ host is able to effectively reduce polarization and achieve a very notable sulfur transformation.

S@NG/WSe₂ cathodes were also tested within cells containing even lower volumes of electrolyte ($7.8 \text{ mL g}^{-1}_{\text{Sulfur}}$) to increase the overall LSB energy density. In these lean electrolyte conditions, the high electrolyte viscosity usually reduces the Li-ion mobility and thus increases the polarization voltage (Figure S26c, Supporting Information). Nevertheless, the S@NG/WSe₂ electrode tested with just $7.8 \text{ mL g}^{-1}_{\text{Sulfur}}$ electrolyte endured 350 cycles with notable stability, showing capacity retention of 65.4%. In addition, the more rigorous electrolyte usage condition, $4.8 \text{ mL g}^{-1}_{\text{Sulfur}}$, was also tested, and the results showed that the lean-electrolyte cell could also run steadily (Figure S26d, Supporting Information). For comparison, the key LSB performance parameters of several state-of-the-art sulfur hosts are listed in Table S1, Supporting Information. Among the numerous sulfur hosts developed as cathode materials in LSBs, NG/WSe₂ exhibits an outstanding capacity and stability.

Finally, to demonstrate the potential for practical use of S@NG/WSe₂ cathodes, we scaled them up to the production of pouch cells (see fabrication details and schematic diagram in the supporting information, Figure S27a, Supporting Information). The initial capacity of the pouch cell based on an S@NG/WSe₂ cathode at 0.25 C was $\approx 800 \text{ mAh g}^{-1}$, and it retained 93.5% of its capacity after 70 cycles (Figure 5h and Figure S27b, Supporting Information). As a demonstration of its power, the pouch cell was able to light a “2021” panel composed of 58 red LED bulbs (Figure 5i; Video S1, Supporting Information). High-sulfur loading and lean electrolyte test were also conducted at the pouch cell level. As displayed in Figure S28, Supporting Information, the S@NG/WSe₂ cathode maintained a stable capacity under 4.3 mg cm^{-2} sulfur loading and $5.8 \text{ mL g}^{-1}_{\text{Sulfur}}$ electrolyte usage, illustrating the potential for practical application of sulfur cathodes based on NG/WSe₂ superlattice hosts.

3. Conclusion

In summary, we reported the scalable synthesis of a superlattice material (NG/WSe₂) by a simple two-step method and its application as sulfur host in LSBs. The synthesis method involved a first solvothermal process that resulted in hybrid organic-inorganic polymer-WSe₂ superlattices. A subsequent thermal treatment pyrolyzed the polymer to yield NG/WSe₂ superlattices. The temperature of the calcination step allowed a continuous adjustment of the WSe₂ interlayer space, from 10.4 to 21 Å. Compared with WSe₂, NG/WSe₂ superlattices showed a metallic character with no gap of states at the Fermi level, a highly enhanced conductivity (over 100 times), and much faster ion diffusion. NG/WSe₂ superlattices also provided accelerated

reaction kinetics of LiPS conversion, with lower overpotentials and higher Li₂S nucleation capacity. Moreover, both experimental results and theoretical calculations proved that NG/WSe₂ superlattices greatly improve the affinity to LiPS at the heterostructure interface by the formation of Li–N and W–S bonds, which effectively inhibits the soluble LiPS shuttle effect. As a result, S@NG/WSe₂ electrodes allowed a high sulfur utilization, a superior rate performance (569.5 mAh g⁻¹ at 5 C), and improved cycling stability with 81.3% capacity retention after 500 cycles. Even at high sulfur loading, lean electrolyte conditions, and in up-scaled 0.1 Ah capacity pouch cells, robust Li–S performances were demonstrated. All these results demonstrate the excellent qualities of heterostructured superlattices as sulfur hosts in LSB cathodes. Thus, this work not only established a simple, cost-effective, and scalable procedure to produce these materials but also pioneered their use and demonstrated their great potential in the LSB technological field.

4. Experimental Section

Preparing r-WSe₂, WSe₂-800, p-WSe₂, and NG/WSe₂: p-WSe₂ nanosheets were prepared by a one-pot solvothermal method. NG/WSe₂ nanosheets were obtained by the calcination of p-WSe₂ within a controlled atmosphere. Typically, 158 mg of selenium powder and 80 mg of sodium borohydride (NaBH₄) were dissolved in 15 mL N, N-dimethylformamide (DMF), and the mixture was continuously stirred for about 30 min until a dark brown solution (Solution A) was obtained. Solution B was obtained by dissolving 248 mg of AMT and 350 mg PVP in 15 mL DMF with 15 min of stirring. Subsequently, Solution B was poured into Solution A and the mixture was stirred for 5 min. Then, the resultant solution was transferred into an autoclave, which was sealed, and heated at 240 °C for 24 h. After cooling down naturally, the black product was washed with DMF, ethanol, and deionized water several times to remove the precursor residues. The obtained produce was then freeze-dried for 24 h to obtain p-WSe₂ nanosheets. For calcination, the obtained black powder was sealed in a small quartz tube filled with Ar gas, and heated for 2 h at 800 °C with a 5 °C min⁻¹ heating rate to obtain ≈290 mg NG/WSe₂ nanosheets with a yield of 84.8% (calculated based on the quantity of W and Se precursor used). Other calcined products were prepared by the same process but varying the calcination temperatures and they were named p-WSe₂-X (X = calcination temperature). The r-WSe₂ and WSe₂-800 nanosheets were obtained by the same process but without adding PVP. N-carbon was prepared by annealing PVP powder under 800 °C with Ar gas protection with a 5 °C min⁻¹ heating rate.

Preparing of XX-WSe₂ and XX-WSe₂-800 Nanosheets (XX = CTAB, SDS, F127, GLU): XX-WSe₂ and XX-WSe₂-800 samples were obtained by the same methods of p-WSe₂ and NG/WSe₂ nanosheets preparation, but employing another organic/polymer to replace PVP.

Supporting Information

Supporting Information is available from the Wiley Online Library or from the author.

Acknowledgements

This work was supported by the European Regional Development Funds and by the Spanish Ministerio de Economía Competitividad through the projects ENE2016-77798-C4-3-R, and ENE2017-85087-C3. C.Q.Z., B.F., and D.W.Y. thanks the China Scholarship Council for the scholarship support. Authors acknowledge funding from Generalitat de

Catalunya 2017 SGR 327 and 2017 SGR 1246. H.B.Z. thanks the National Natural Science Foundation of China (No. 52073061, 51872048) and Natural Science Foundation of Fujian Province (No. 2021J02020). The computational work was supported by the Welch Foundation (F-1841) and the Texas Advanced Computing Center.

Conflict of Interest

The authors declare no conflict of interest.

Data Availability Statement

The data that support the findings of this study are available from the corresponding author upon reasonable request.

Keywords

heterostructures, lithium polysulfides, lithium–sulfur batteries, superlattice, tungsten selenide

Received: February 1, 2022

Revised: February 24, 2022

Published online:

- [1] K. S. Novoselov, A. K. Geim, S. V. Morozov, D. Jiang, Y. Zhang, S. V. Dubonos, I. V. Grigorieva, A. A. Firsov, *Science* **2004**, *306*, 666.
- [2] Q. Yun, L. Li, Z. Hu, Q. Lu, B. Chen, H. Zhang, *Adv. Mater.* **2020**, *32*, 1903826.
- [3] C. Tan, X. Cao, X.-J. Wu, Q. He, J. Yang, X. Zhang, J. Chen, W. Zhao, S. Han, G.-H. Nam, M. Sindoro, H. Zhang, *Chem. Rev.* **2017**, *117*, 6225.
- [4] K. S. Novoselov, A. Mishchenko, A. Carvalho, A. H. Castro Neto, *Science* **2016**, *353*, aac9439.
- [5] P. Xiong, B. Sun, N. Sakai, R. Ma, T. Sasaki, S. Wang, J. Zhang, G. Wang, *Adv. Mater.* **2020**, *32*, 1902654.
- [6] Y. Huang, J. Liang, C. Wang, S. Yin, W. Fu, H. Zhu, C. Wan, *Chem. Soc. Rev.* **2020**, *49*, 6866.
- [7] A. Khan, J. Azadmanjiri, B. Wu, L. Liping, Z. Sofer, J. Min, *Adv. Energy Mater.* **2021**, *11*, 2100451.
- [8] G. Jin, C.-S. Lee, O. F. N. Okello, S.-H. Lee, M. Y. Park, S. Cha, S.-Y. Seo, G. Moon, S. Y. Min, D.-H. Yang, C. Han, H. Ahn, J. Lee, H. Choi, J. Kim, S.-Y. Choi, M.-H. Jo, *Nat. Nanotechnol.* **2021**, *16*, 1092.
- [9] C. Forsythe, X. Zhou, K. Watanabe, T. Taniguchi, A. Pasupathy, P. Moon, M. Koshino, P. Kim, C. R. Dean, *Nat. Nanotechnol.* **2018**, *13*, 566.
- [10] P. Xiong, X. Zhang, H. Wan, S. Wang, Y. Zhao, J. Zhang, D. Zhou, W. Gao, R. Ma, T. Sasaki, G. Wang, *Nano Lett.* **2019**, *19*, 4518.
- [11] Y. Guo, Q. Chen, A. Nie, H. Yang, W. Wang, J. Su, S. Wang, Y. Liu, S. Wang, H. Li, Z. Liu, T. Zhai, *ACS Nano* **2020**, *14*, 1635.
- [12] J. Zhuang, C. Liu, Q. Gao, Y. Liu, H. Feng, X. Xu, J. Wang, J. Zhao, S. X. Dou, Z. Hu, Y. Du, *ACS Nano* **2018**, *12*, 5059.
- [13] Y. Shen, Y. Wang, Y. Miao, M. Yang, X. Zhao, X. Shen, *Adv. Mater.* **2020**, *32*, 1905524.
- [14] M. S. Islam, M. Kim, X. Jin, S. M. Oh, N.-S. Lee, H. Kim, S.-J. Hwang, *ACS Energy Lett.* **2018**, *3*, 952.
- [15] C. Wang, N. Sakai, Y. Ebina, T. Kikuchi, M. R. Snowdon, D. Tang, R. Ma, T. Sasaki, *J. Mater. Chem. A* **2021**, *9*, 9952.
- [16] L. Ji, M. Rao, H. Zheng, L. Zhang, Y. Li, W. Duan, J. Guo, E. J. Cairns, Y. Zhang, *J. Am. Chem. Soc.* **2011**, *133*, 18522.

- [17] H. Wang, Q. Zhang, H. Yao, Z. Liang, H.-W. Lee, P.-C. Hsu, G. Zheng, Y. Cui, *Nano Lett.* **2014**, *14*, 7138.
- [18] Z. A. Ghazi, X. He, A. M. Khattak, N. A. Khan, B. Liang, A. Iqbal, J. Wong, H. Sin, L. Li, Z. Tang, *Adv. Mater.* **2017**, *29*, 1606817.
- [19] B. Fei, C. Zhang, D. Cai, J. Zheng, Q. Chen, Y. Xie, L. Zhu, A. Cabot, H. Zhan, *ACS Nano* **2021**, *15*, 6849.
- [20] C. Zhang, R. Du, J. J. Biendicho, M. Yi, K. Xiao, D. Yang, T. Zhang, X. Wang, J. Arbiol, J. Llorca, Y. Zhou, J. R. Morante, A. Cabot, *Adv. Energy Mater.* **2021**, *11*, 2100432.
- [21] Z. Liang, D. Yang, P. Tang, C. Zhang, J. J. Biendicho, Y. Zhang, J. Llorca, X. Wang, J. Li, M. Heggen, J. David, R. E. Dunin-Borkowski, Y. Zhou, J. R. Morante, A. Cabot, J. Arbiol, *Adv. Energy Mater.* **2021**, *11*, 2003507.
- [22] G. Babu, N. Masurkar, H. Al Salem, L. M. R. Arava, *J. Am. Chem. Soc.* **2017**, *139*, 171.
- [23] H. Lin, L. Yang, X. Jiang, G. Li, T. Zhang, Q. Yao, G. W. Zheng, J. Y. Lee, *Energy Environ. Sci.* **2017**, *10*, 1476.
- [24] H.-J. Li, K. Xi, W. Wang, S. Liu, G.-R. Li, X.-P. Gao, *Energy Storage Mater.* **2022**, *45*, 1229.
- [25] P. Wang, F. Sun, S. Xiong, Z. Zhang, B. Duan, C. Zhang, J. Feng, B. Xi, *Angew. Chem.* **2021**, *134*, e202116048.
- [26] S. Zhou, S. Liu, W. Chen, Y. Cheng, J. Fan, L. Zhao, X. Xiao, Y.-H. Chen, C.-X. Luo, M.-S. Wang, T. Mei, X. Wang, H.-G. Liao, Y. Zhou, L. Huang, S.-G. Sun, *ACS Nano* **2021**, *15*, 13814.
- [27] R. Bryaskova, D. Pencheva, S. Nikolov, T. Kantardjiev, *J. Chem. Biol.* **2011**, *4*, 185.
- [28] L. Mo, Z. Guo, Z. Wang, L. Yang, Y. Fang, Z. Xin, X. Li, Y. Chen, M. Cao, Q. Zhang, L. Li, *Nanoscale Res. Lett.* **2019**, *14*, 197.
- [29] Y. Liu, Y. Qiao, W.-X. Zhang, Z. Li, X.-L. Hu, L.-X. Yuan, Y.-H. Huang, *J. Mater. Chem.* **2012**, *22*, 24026.
- [30] P. D. Antunez, D. H. Webber, R. L. Brutchey, *Chem. Mater.* **2013**, *25*, 2385.
- [31] P. Xiong, R. Ma, N. Sakai, L. Nurdiwijayanto, T. Sasaki, *ACS Energy Lett.* **2018**, *3*, 997.
- [32] D. Bennett, B. Remez, *npj 2D Mater. Appl.* **2022**, *6*, 7.
- [33] X. Luo, Y. Zhao, J. Zhang, M. Toh, C. Kloc, Q. Xiong, S. Y. Quek, *Phys. Rev. B* **2013**, *88*, 195313.
- [34] H. Liu, B. Liu, H. Guo, M. Liang, Y. Zhang, T. Borjigin, X. Yang, L. Wang, X. Sun, *Nano Energy* **2018**, *51*, 639.
- [35] X. Hu, Y. Liu, J. Li, G. Wang, J. Chen, G. Zhong, H. Zhan, Z. Wen, *Adv. Funct. Mater.* **2020**, *30*, 1907677.
- [36] C. Zhang, Q. Chen, H. Zhan, *ACS Appl. Mater. Interfaces* **2016**, *8*, 22977.
- [37] F. Han, J. Yue, X. Fan, T. Gao, C. Luo, Z. Ma, L. Suo, C. Wang, *Nano Lett.* **2016**, *16*, 4521.
- [38] Z. Lin, Z. Wan, F. Song, B. Huang, C. Jia, Q. Qian, J. S. Kang, Y. Wu, X. Yan, L. Peng, C. Wan, J. Zhou, Z. Sofer, I. Shakir, Z. Almutairi, S. Tolbert, X. Pan, Y. Hu, Y. Huang, X. Duan, *Chem* **2021**, *7*, 1887.
- [39] W. Yu, Z. Dong, I. Abdelwahab, X. Zhao, J. Shi, Y. Shao, J. Li, X. Hu, R. Li, T. Ma, Z. Wang, Q.-H. Xu, D. Y. Tang, Y. Song, K. P. Loh, *ACS Nano* **2021**, *15*, 18448.
- [40] J. Ni, W. Wang, M. Quintana, F. Jia, S. Song, *Appl. Surf. Sci.* **2020**, *514*, 145911.
- [41] Y. Wang, R. Zhang, Z. Sun, H. Wu, S. Lu, J. Wang, W. Yu, J. Liu, G. Gao, S. Ding, *Adv. Mater. Interfaces* **2020**, *7*, 1902092.
- [42] D. Sun, K. Liu, J. Hu, J. Zhou, *Small* **2021**, *17*, 2006374.
- [43] C. Zhang, J. J. Biendicho, T. Zhang, R. Du, J. Li, X. Yang, J. Arbiol, Y. Zhou, J. R. Morante, A. Cabot, *Adv. Funct. Mater.* **2019**, *29*, 1903842.
- [44] J. Liu, Y. Zhang, L. Zhang, F. Xie, A. Vasileff, S.-Z. Qiao, *Adv. Mater.* **2019**, *31*, 1901261.
- [45] X. Hong, J. Jin, T. Wu, Y. Lu, S. Zhang, C. Chen, Z. Wen, *J. Mater. Chem. A* **2017**, *5*, 14775.
- [46] D. Yang, Z. Liang, C. Zhang, J. J. Biendicho, M. Botifoll, M. C. Spadaro, Q. Chen, M. Li, A. Ramon, A. O. Moghaddam, J. Llorca, J. Wang, J. R. Morante, J. Arbiol, S.-L. Chou, A. Cabot, *Adv. Energy Mater.* **2021**, *11*, 2101250.
- [47] Z. Yi, F. Su, L. Huo, G. Cui, C. Zhang, P. Han, N. Dong, C. Chen, *Appl. Surf. Sci.* **2020**, *503*, 144446.
- [48] J. He, G. Hartmann, M. Lee, G. S. Hwang, Y. Chen, A. Manthiram, *Energy Environ. Sci.* **2019**, *12*, 344.
- [49] D. Yang, C. Zhang, J. J. Biendicho, X. Han, Z. Liang, R. Du, M. Li, J. Li, J. Arbiol, J. Llorca, Y. Zhou, J. R. Morante, A. Cabot, *ACS Nano* **2020**, *14*, 15492.
- [50] Z. Yuan, H.-J. Peng, T.-Z. Hou, J.-Q. Huang, C.-M. Chen, D.-W. Wang, X.-B. Cheng, F. Wei, Q. Zhang, *Nano Lett.* **2016**, *16*, 519.
- [51] L. Ma, W. Zhang, L. Wang, Y. Hu, G. Zhu, Y. Wang, R. Chen, T. Chen, Z. Tie, J. Liu, Z. Jin, *ACS Nano* **2018**, *12*, 4868.
- [52] F. Liu, G. Sun, H. B. Wu, G. Chen, D. Xu, R. Mo, L. Shen, X. Li, S. Ma, R. Tao, X. Li, X. Tan, B. Xu, G. Wang, B. S. Dunn, P. Sautet, Y. Lu, *Nat. Commun.* **2020**, *11*, 5215.
- [53] S. Wang, S. Feng, J. Liang, Q. Su, F. Zhao, H. Song, M. Zheng, Q. Sun, Z. Song, X. Jia, J. Yang, Y. Li, J. Liao, R. Li, X. Sun, *Adv. Energy Mater.* **2021**, *11*, 2003314.
- [54] X. Tao, J. Wang, C. Liu, H. Wang, H. Yao, G. Zheng, Z. W. Seh, Q. Cai, W. Li, G. Zhou, C. Zu, Y. Cui, *Nat. Commun.* **2016**, *7*, 11203.
- [55] W. Chen, T. Lei, W. Lv, Y. Hu, Y. Yan, Y. Jiao, W. He, Z. Li, C. Yan, J. Xiong, *Adv. Mater.* **2018**, *30*, 1804084.
- [56] X. Zhu, W. Zhao, Y. Song, Q. Li, F. Ding, J. Sun, L. Zhang, Z. Liu, *Adv. Energy Mater.* **2018**, *8*, 1800201.
- [57] G. Zhou, H. Tian, Y. Jin, X. Tao, B. Liu, R. Zhang, Z. W. Seh, D. Zhuo, Y. Liu, J. Sun, J. Zhao, C. Zu, D. S. Wu, Q. Zhang, Y. Cui, *Proc. Natl. Acad. Sci. U. S. A.* **2017**, *114*, 840.
- [58] X. Chen, L. Peng, L. Wang, J. Yang, Z. Hao, J. Xiang, K. Yuan, Y. Huang, B. Shan, L. Yuan, J. Xie, *Nat. Commun.* **2019**, *10*, 1021.
- [59] S. Li, W. Zhang, Z. Zeng, S. Cheng, J. Xie, *Electrochem. Energy Rev.* **2020**, *3*, 613.
- [60] Z. Guo, H. Nie, Z. Yang, W. Hua, C. Ruan, D. Chan, M. Ge, X. Chen, S. Huang, *Adv. Sci.* **2018**, *5*, 1800026.
- [61] W. Bao, D. Su, W. Zhang, X. Guo, G. Wang, *Adv. Funct. Mater.* **2016**, *26*, 8746.
- [62] Y. Lu, J.-L. Qin, T. Shen, Y.-F. Yu, K. Chen, Y.-Z. Hu, J.-N. Liang, M.-X. Gong, J.-J. Zhang, D.-L. Wang, *Adv. Energy Mater.* **2021**, *11*, 2101780.
- [63] S. Waluś, C. Barchasz, R. Bouchet, F. Alloin, *Electrochim. Acta* **2020**, *359*, 136944.
- [64] A. Schneider, C. Weidmann, C. Suchomski, H. Sommer, J. Janek, T. Brezesinski, *Chem. Mater.* **2015**, *27*, 1674.
- [65] J. Wang, Z. Zhang, X. Yan, S. Zhang, Z. Wu, Z. Zhuang, W.-Q. Han, *Nano-Micro Lett.* **2019**, *12*, 4.